# Electric Field Alignment in Thin Films of Cylinder-Forming Diblock Copolymer

**M. W. Matsen***

*Department of Physics, University of Reading, Whiteknights, Reading RG6 6AF, United Kingdom*

*Received March 2, 2006; Revised Manuscript Received May 11, 2006*

ABSTRACT: We investigate thin films of cylinder-forming diblock copolymer confined between electrically charged parallel plates, using self-consistent-field theory (SCFT) combined with an exact treatment for linear dielectric materials. Our study focuses on the competition between the surface interactions, which tend to orient cylinder domains parallel to the plates, and the electric field, which favors a perpendicular orientation. The effect of the electric field on the relative stability of the competing morphologies is demonstrated with equilibrium phase diagrams, calculated with the aid of a weak-field approximation. As hoped, modest electric fields are shown to have a significant stabilizing effect on perpendicular cylinders, particularly for thicker films. Our improved SCFT-based treatment removes most of the approximations implemented by previous approaches, thereby managing to resolve outstanding qualitative inconsistencies among different approximation schemes.

## I. Introduction

The natural self-assembly of block copolymer thin films into periodically ordered morphologies offers an efficient means of fabricating nanoscale structures.[1] Proposed applications include the construction of high-capacity data-storage devices, waveguides, quantum dot arrays, dielectric mirrors, nanoporous membranes, and nanowires. Although the self-assembly process is exceptionally efficient, it does not always produce the desired pattern. For instance, lamellar and cylindrical domains tend to orient parallel to the substrate due to surface interactions, as opposed to perpendicular where they would exhibit a more useful lateral structure. A possible solution to the problem was suggested by Amundson et al.,[2] when they demonstrated that block copolymer microstructures respond to electric fields that couple to the dielectric contrast between the different domains. Indeed, Russell and co-workers have since used electric fields to align both lamellar[3] and cylindrical[4,5] domains in thin films of poly(styrene)−poly(methyl methacrylate) (PS−PMMA) diblock copolymer. It has been suggested by Tsori et al.[6] that the alignment is primarily mediated by free $Li^+$ ions within the PMMA domains, although recent experimental work by Wang et al.[7] sheds some doubt on this. In any case, we will restrict our attention to diblock species for which the dielectric mechanism is dominant.

Theoretical work on the dielectric mechanism in thin films initially focused on simple lamellar morphologies. Pereira and Williams[8] were the first to examine the competition between parallel and perpendicular orientations as a function of film thickness, surface interactions, and electric-field strength, and they were able to do so with a simple analytical treatment based on the strong-stretching theory (SST) of Semenov.[9] Key to this analytical treatment is the fact that the electric field direction remains strictly perpendicular to the film, which allows the lamellar domains to be represented as individual capacitors in an electrical circuit, joined together in series or parallel depending on the orientation of the domains. Ashok et al.[10] and Tsori and Andleman[11] have also performed similar calculations on thin films of lamellar-forming diblock copolymer using this SST-based treatment.

* E-mail: m.w.matsen@reading.ac.uk.

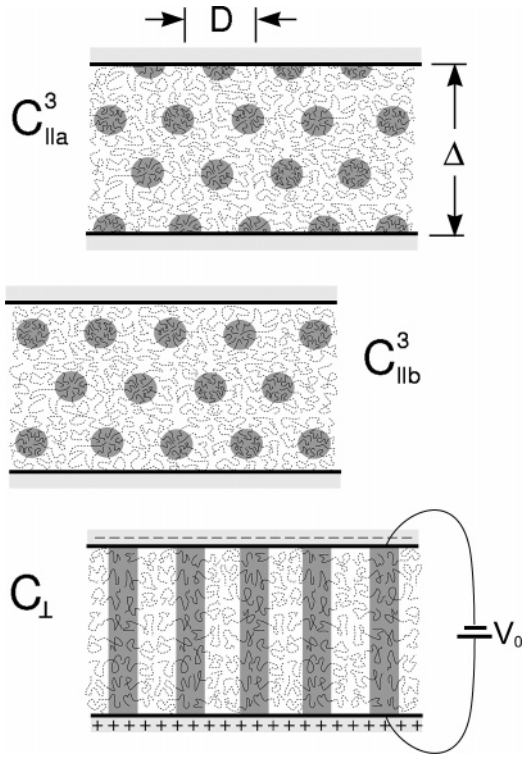


**Figure 1.** Cylinder-forming diblock copolymer confined between two conducting plates. The parallel morphologies ($C^\nu_{\|a}$ and $C^\nu_{\|b}$) are favored by surface affinities for the minority and majority components, respectively. (The superscript $\nu$ refers to the number of complete cylinder layers.) The perpendicular phase ($C_\perp$) is favored by the application of an electric field, $E_0 = V_0/\Delta$.

Unfortunately, the SST approach is not so amenable to nonlamellar structures, and even the comparatively simple cylinder morphologies illustrated in Figure 1 have proven to be immensely more difficult. This is evident from studies by Pereira[12] comparing the relative stability of the $C^\nu_{\|a}$ and $C_\perp$ phases between plates with a mild affinity for the minority component and by Ashok et al.[10] examining the $C^\nu_{\|b}$ and $C_\perp$ morphologies for plates favoring the matrix component. Both studies were faced with a dilemma of what to assume for the

10.1021/ma060456m CCC: $33.50 
Published on Web 06/27/2006

precise shape of the cylindrical domains, whereas it had been sufficient to assume simple flat interfaces for the previous lamellar structures. Furthermore, the electric field deviated from the perpendicular direction, causing the capacitor analogy to break down. Pereira performed the more extensive of the two studies, investigating a variety of approximations for the interfacial shape, for the entropic stretching energy of the polymer chains, and for the electrostatic energy. Ideally, the choice of approximations should only have a mild quantitative effect on the predictions, but in fact the variation was so great that not even the qualitative behavior was consistent. For example, one approximation scheme predicted the electric field to favor the $C_\perp$ phase, while another predicted the opposite under identical conditions. With such serious inconsistencies, there is a clear need for a more refined treatment.

Here we revisit thin films of cylinder-forming diblock copolymer, but now using the self-consistent-field theory (SCFT) of Helfand.[13] This provides exact mean-field predictions where, for example, the domain shape adjusts automatically to minimize the free energy. We also solve the Maxwell equations for the electric field exactly, under the assumption that the polymer behaves as a linear dielectric material.[14,15] The only price of removing the numerous approximations invoked by the previous SST treatments is that the SCFT has to be performed numerically, although this is not a big loss given the complexity of the analytical SST expressions. In any case, the slight disadvantage of the numerical approach is diminished by invoking a weak-field approximation that slashes the computational demands of the SCFT calculation, while simultaneously providing significant transparency for how the surface interactions and electric field impact the behavior of the film.

## II. Theory

This section incorporates an applied electric field into the SCFT of ref 16 for a melt of $n$ AB diblock copolymer molecules confined between two parallel plates of area, $\mathcal{A}$, at $z = 0$ and $\Delta$. As before, we assume that each diblock contains $fN$ A-type segments joined to $(1 - f)N$ B-type segments, where all segments have a statistical length of $a$ and are incompressible with a volume of $\rho_0^{-1}$ such that total volume of the melt is $\mathcal{V} \equiv \mathcal{A}\Delta = nN/\rho_0$. The interaction between A and B segments is controlled by the usual Flory−Huggins $\chi$ parameter. Following similar steps to those in ref 16, the partition function of the system is expressed as

$$Z \propto \int \mathcal{D}\Phi_A \mathcal{D}W_A \mathcal{D}W_B \exp\left(-\frac{F[\Phi_A,W_A,W_B]}{k_BT}\right) \quad (1)$$

where

$$\frac{F[\Phi_A,W_A,W_B]}{nk_BT} \equiv -\ln \mathcal{Q}[W_A,W_B] - \frac{1}{\mathcal{V}}\int d\mathbf{r}\{\chi N\Phi_A(\mathbf{r}) + W_A(\mathbf{r}) - W_B(\mathbf{r}) - 2H(\mathbf{r})N\}\Phi_A(\mathbf{r}) - \mathcal{E} \quad (2)$$

and $\mathcal{Q}[W_A,W_B]$ is the partition function of a single diblock copolymer with the fields, $W_A(\mathbf{r})$ and $W_B(\mathbf{r})$, acting on its A and B segments, respectively. Be aware that we have made a few changes to the original expressions in ref 16. First, we have followed an equivalent but slightly simplified derivation,[18] where only three auxiliary functions, $\Phi_A(\mathbf{r})$, $W_A(\mathbf{r})$, and $W_B(\mathbf{r})$, are introduced into eq 1 instead of five. Second, isolated terms of $\Phi_A(\mathbf{r})$ have been dropped from eq 2 because they integrate to a constant and thus have no effect.

Further simplification is achieved by setting the width over which the polymer concentration vanishes near the confining plates (the $\epsilon$ in ref 16) to zero. With that, the surface potential[17] reduces to

$$H(\mathbf{r}) = 2\{\Lambda_1\delta(z) + \Lambda_2\delta(z - \Delta)\}aN^{1/2} \quad (3)$$

Note that the Dirac delta functions in eq 3 lie directly on the boundaries, and thus the polymer film only experiences half of their weight, which is the reason for the prefactor of 2. The main advantage of the step profile is that it equates to reflecting boundary conditions,[18,19] which reduce the numerical demands and introduce a useful symmetry into some of the calculations. The only slight consequence is the loss of a small negative line tension that favors the intersection of the block copolymer interfaces with the confining plates.[16]

The most significant change to the theory in ref 16 is the extra term

$$\mathcal{E} = \frac{\epsilon_0 E_0^{\,2}}{2nk_BT}\int d\mathbf{r}\, \kappa(\mathbf{r})|\nabla v(\mathbf{r})|^2 \quad (4)$$

in eq 2 that couples the electric permittivity of the morphology

$$\kappa(\mathbf{r}) = \kappa_A\Phi_A(\mathbf{r}) + \kappa_B(1 - \Phi_A(\mathbf{r})) \quad (5)$$

to the electric field

$$\mathbf{E}(\mathbf{r}) = -E_0\nabla v(\mathbf{r}) \quad (6)$$

produced by the voltage difference, $V_0 = E_0\Delta$, across the conducting plates. The scaled electric potential, $v(\mathbf{r})$, satisfies the Maxwell equation

$$\nabla\cdot\{\kappa(\mathbf{r})\nabla v(\mathbf{r})\} = 0 \quad (7)$$

with the fixed boundary conditions: $v = 0$ at $z = 0$ and $v = -\Delta$ at $z = \Delta$. While SST calculations[10,12] only depend on the permittivities, $\kappa_A$ and $\kappa_B$, for the pure components, SCFT calculations require $\kappa(\mathbf{r})$ for the entire composition range, $0 \le \Phi_A(\mathbf{r}) \le 1$. Equation 5 calculates this on the basis of the usual simple-mixing assumption,[2,4,6,11,15] and this should be more than adequate apart from perhaps the weak-segregation regime where there is significant mixing throughout the morphology.[21]

Following the standard saddle-point approximation of SCFT, the free energy of the system is approximated by the extrema of $F[\Phi_A,W_A,W_B]$, denoted by the functions $\phi_A(\mathbf{r})$, $w_A(\mathbf{r})$, and $w_B(\mathbf{r})$. Setting the functional derivative of $F$ with respect to $W_A(\mathbf{r})$ to zero identifies $\phi_A(\mathbf{r})$ as the A-segment concentration, while differentiation with respect to $W_B(\mathbf{r})$ gives the incompressibility condition

$$\phi_A(\mathbf{r}) + \phi_B(\mathbf{r}) = 1 \quad (8)$$

where $\phi_B(\mathbf{r})$ is identified as the B-segment concentration. The remaining differentiation with respect to $\Phi_A(\mathbf{r})$ produces the self-consistent-field equation

$$w_A(\mathbf{r}) - w_B(\mathbf{r}) = -2\chi N\phi_A(\mathbf{r}) - 2H(\mathbf{r})N - 2\kappa_\Delta\mathcal{E}_D|\nabla v(\mathbf{r})|^2 \quad (9)$$

where

$$\mathcal{E}_D \equiv \frac{\epsilon_0\bar{\kappa}E_0^{\,2}\mathcal{V}}{2nk_BT} \quad (10)$$

is the value of $\mathcal{C}$ for a disordered film and

$$\kappa_\Delta \equiv \frac{\kappa_A - \kappa_B}{2\bar{\kappa}} \tag{11}$$

$$\bar{\kappa} \equiv f\kappa_A + (1-f)\kappa_B \tag{12}$$

specify the dielectric contrast and the average dielectric constant, respectively. Note that eq 9 is simplified by the fact that the functional derivate of $\mathcal{C}$ with respect to $v(\mathbf{r})$ at fixed $\kappa(\mathbf{r})$ is zero.[14]

Rather than solve the SCFT equations in real space, we follow a spectral (i.e., Fourier) technique detailed in ref 14. The main advantage is that the Maxwell eq 7 can be solved by a simple matrix inversion that adds virtually nothing to the computational demands of a standard SCFT calculation. Furthermore, some simplification to the self-consistent-field eq 9 can be achieved by using an alternative expression for the electrostatic energy in eq 4. Because the spectral approach allows many of the steps to be performed analytically, the only significant source of numerical inaccuracy is in the truncation of large wavevectors. However, we are careful to retain a sufficient number of Fourier terms such that all inaccuracies are undetectable at the resolution of our plots.

## III. Results

At first count, the diblock copolymer melt confined between charged plates constitutes an enormous 12-dimensional parameter space: $T$, $n$, $N$, $a$, $f$, $\chi$, $\Delta$, $\Lambda_1$, $\Lambda_2$, $\kappa_A$, $\kappa_B$, and $V_0$. Fortunately, the various scaling relations reduces this space to seven dimensions: $f$, $\chi N$, $\Delta/aN^{1/2}$, $\Lambda_1 N$, $\Lambda_2 N$, $\kappa_\Delta$, and $\mathcal{C}_D$. Still this is too much to contend with in a single paper, and so we make a few judicious restrictions. First, we set the diblock composition to $f = 0.25$, which is near the middle of the cylindrical region of the bulk phase diagram.[20] Second, we fix the degree of segregation at $\chi N = 25$, which is a level characteristic of experiment and one where the intrinsic behavior of a microphase-separated morphology is governed by a competition between the entropic penalty of chain stretching and the unfavorable interfacial tension.[22] Third, we assume both confining plates are identical, which implies $\Lambda_1 = \Lambda_2 \equiv \Lambda$. With that, the parameter space is reduced to a manageable four dimensions: $\Delta/D_b$, $\Lambda N$, $\kappa_\Delta$, and $\mathcal{C}_D$. To aid the interpretation of the results, we measure distances (e.g., $\Delta$ and $D$) in terms of the bulk nearest-neighbor cylinder spacing, $D_b = 1.6847aN^{1/2}$. Similarly, we measure the free energy of the film, $F$, relative to that of the bulk cylinder phase, $F_b$.

We begin by examining films confined between completely neutral plates, both chemically and electrically (i.e., $\Lambda N = \mathcal{C}_D = 0$), conditions under which the $C_\perp$ and $C^\nu_{||a}$ phases depicted in Figure 1 compete for stability. Because the plates behave as reflecting boundaries, the $C_\perp$ phase is equivalent to the bulk cylinder phase, and thus its free energy is $F = F_b$ and its lateral periodicity is $D = D_b$. Of course, the $C^\nu_{||a}$ phases are strongly affected by the confinement given the obvious constraint the film thickness, $\Delta$, places on the cylinder spacing. This is illustrated in Figure 2 for films with $\nu = 2$ complete cylinder layers. Small values of $\Delta$ force the cylinders apart in the lateral direction resulting in a large periodicity, $D$. As $\Delta$ increases, the lateral spacing gradually relaxes up until $D \approx D_b$. Beyond that, $D$ remains relatively constant while the aspect ratio of the cylinders, $R_\perp/R_{||}$, diverges, transforming them into lamellar-like domains. Notice that for zero surface affinity the minority A-rich domains along the plates remain exactly the same as the cylinders in the middle of the film, but cut in half.

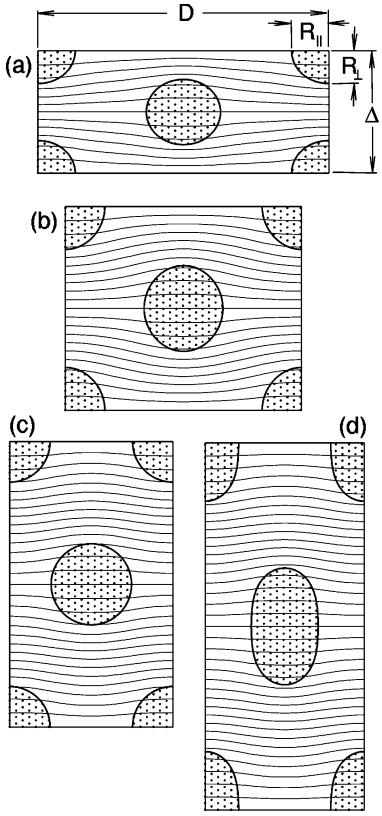


**Figure 2.** One complete period, $D$, of the $C^2_{||a}$ phase confined between inert plates (i.e., $\Lambda N = 0$) separated by (a) $\Delta/D_b = 0.75$, (b) 1.25, (c) 1.75, and (d) 2.25. The bold curves denote A/B interfaces defined by $\phi_A(\mathbf{r}) = 0.5$, while the horizontal curves show equipotential contours at equal intervals of $\delta v = D_b/16$ calculated in the weak-field limit (i.e., $\mathcal{C}_D \to 0$) for a dielectric contrast of $\kappa_\Delta = 0.5$.

Figure 3 plots the effect of film thickness on the free energy $F_0$, lateral periodicity $D$, and the cylinder aspect ratio $R_\perp/R_{||}$ of the $C^\nu_{||a}$ phases. The curves for different numbers $\nu$ of cylinder layers become identical when plotted as a function of $\Delta/\nu$ because the $C^\nu_{||a}$ morphologies exhibit mirror symmetry planes at $z = i\Delta/\nu$, for $i = 1, 2, ..., \nu - 1$. (This symmetry would be slightly broken had we not implemented the simplified reflecting boundary conditions at $z = 0$ and $\Delta$.) At the special thicknesses, $2\Delta/\nu = D_b$ and $\sqrt{3}D_b$, indicated by the vertical dotted lines, the cylinders adopt the hexagonal packing of the bulk phase with $D = \sqrt{3}D_b$ and $D_b$, respectively. As a consequence, the free energy of the $C^\nu_{||a}$ phases becomes degenerate with that of the $C_\perp$ phase (i.e., $F_0 = F_b$). However, at all other $\Delta$, the distortion from the hexagonal packing results in an elevated free energy (i.e., $F_0 > F_b$), which causes the parallel orientation to be unstable. Incidentally, the free energy peak between the two minima corresponds to a square packing with $\Delta/\nu = D$.

Now we examine the effect of charging the plates while still keeping them chemically neutral. For the $C_\perp$ phase, the electric potential is simply $v(\mathbf{r}) = -z$, and hence the field direction remains strictly perpendicular to the plates. As a consequence, the free energy takes on the simple form $F = F_b - nk_BT\mathcal{C}_D$, while the lateral periodicity $D$ and the morphology $\phi_A(\mathbf{r})$ remain absolutely unaffected. On the other hand, the $C^\nu_{||a}$ phases do respond to the electric field, although the perturbation is generally weak. Figure 3 shows the effect for a field strength of $\mathcal{C}_D = 0.3$ with a dielectric contrast of $\kappa_\Delta = 0.5$. The change in $D$ is too tiny to be resolved on the scale of Figure 3b, but Figure 3c shows a noticeable deformation of the cylinders in the field direction. The most pronounced effect, however, is on

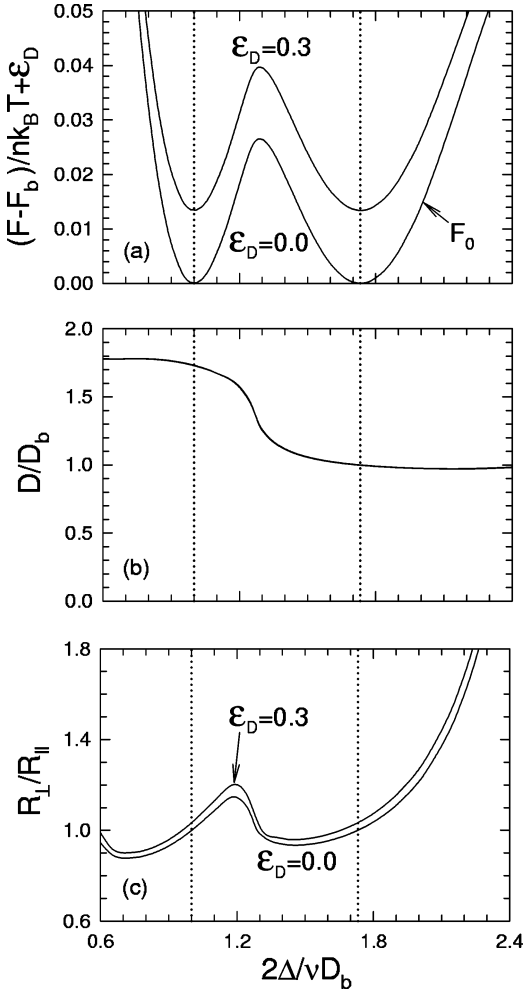


**Figure 3.** Plots for the $C^{\nu}_{||a}$ phases comparing (a) the free energy $F$, (b) the lateral periodicity $D$, and (c) the cylinder aspect ratio $R_{\perp}/R_{||}$ for films with ($\mathcal{E}_D = 0.3$, $\kappa_\Delta = 0.5$) and without ($\mathcal{E}_D = 0.0$) an applied electric field. The vertical dotted lines denote the film thicknesses, $\Delta$, corresponding to hexagonal packing.

the stability of the $C^{\nu}_{||a}$ phases. As demonstrated by Figure 3a, the electric field causes the parallel orientation to become rather unstable, increasing its free energy relative to that of the perpendicular orientation by more than $0.01k_BT$ per molecule.

The mild effect of the electric field on the morphology suggests a useful approximation where the Maxwell equation for $v(\mathbf{r})$ is solved for the zero-field profile, $\phi_A(\mathbf{r})$. Figure 2 shows the resulting equipotential surfaces for a dielectric contrast of $\kappa_\Delta = 0.5$. Notice that the spacing between equipotential surfaces is greater inside the cylinder domains than in the matrix, which implies a weaker electric field as expected given their larger polarizability (i.e., $\kappa_A > \kappa_B$). Once $v(\mathbf{r})$ is calculated, we then evaluate

$$\Omega \equiv \frac{1}{\mathcal{V}\bar{\kappa}}\int d\mathbf{r}\, \kappa(\mathbf{r})|\nabla v(\mathbf{r})|^2 \qquad (13)$$

which approximates the ratio of the electrostatic energy of the $C^{\nu}_{||a}$ phases, $\mathcal{E}$, to that of a disordered film, $\mathcal{E}_D$. Provided that the electric field is not too strong, $F \approx F_0 - nk_BT\Omega\mathcal{E}_D$, where $F_0$ is the zero-field free energy plotted in Figure 3a. As a testament to its accuracy, this weak-field approximation is indistinguishable from the exact result for $\mathcal{E}_D = 0.3$ and $\kappa_\Delta = 0.5$ on the scale of Figure 3a.

The relative electrostatic energy, $\Omega \equiv \mathcal{E}/\mathcal{E}_D$, for the $C^{\nu}_{||a}$ phases in the weak-field limit is plotted as a function of film

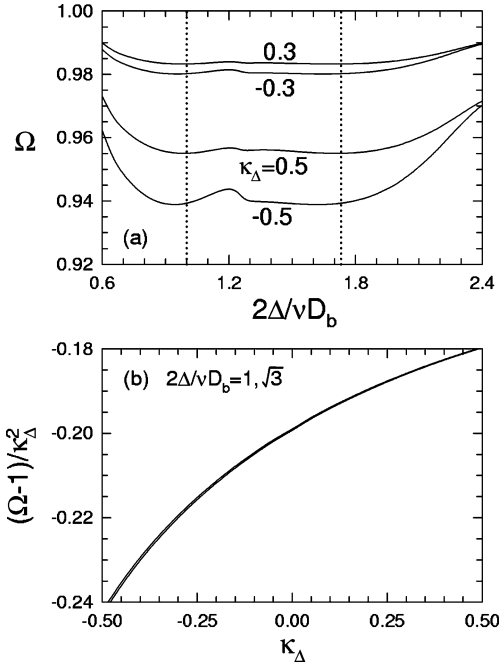


**Figure 4.** Relative electrostatic energy, $\Omega \equiv \mathcal{E}/\mathcal{E}_D$, for the $C^{\nu}_{||a}$ phases in the $\Lambda N = \mathcal{E}_D = 0$ limit. Plot (a) shows the dependence on film thickness, $\Delta$, and plot (b) illustrates the dependence on dielectric contrast, $\kappa_\Delta$, for the two cases of hexagonal packing (i.e., $2\Delta/\nu = D_b$ and $\sqrt{3}D_b$) denoted by the vertical dotted lines in (a).

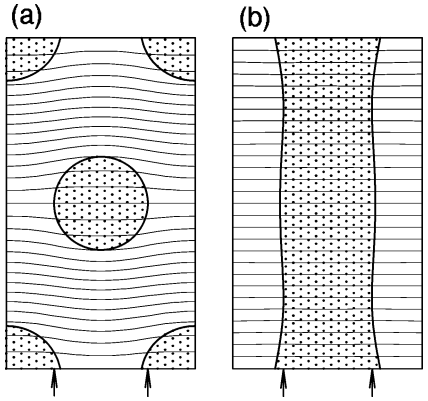


**Figure 5.** Analogous plots to those in Figure 2, but with a surface affinity ($\Lambda N = 0.08$) for the minority domain. Plots (a) and (b) show complete periods of the $C^2_{||a}$ and $C_\perp$ phases, respectively, calculated for a film thickness of $\Delta/D_b = 1.25$. The arrows indicate where the contact points of the A/B interface relax to when the surface affinity is removed (i.e., $\Lambda N = 0$).

thickness in Figure 4a for a series of different dielectric contrasts. In all cases, $\Omega < 1$, which implies that the electric field favors perpendicular cylinders exclusively. For the most part, $\Omega$ has a mild dependence on the film thickness, and in fact, its values at the two free energy minima (i.e., $2\Delta/\nu = D_b$ and $\sqrt{3}D_b$) are virtually identical, as illustrated by Figure 4b. Ignoring the $\Delta$ dependence, $\Omega \approx 1 - 0.2\kappa_\Delta^2 + 0.05\kappa_\Delta^3$ to a reasonable approximation. Notice that the cubic term implies a sensitivity to the sign of $\kappa_\Delta$ that is absent in previous weak-field approximations.[2,4,29]

Next we examine plates with a slight affinity for the minority A-type segments ($\Lambda N = 0.08$) sufficient to stabilize the $C^{\nu}_{||a}$ phases over the $C_\perp$ phase. Figure 5a shows the resulting morphology of the $C^2_{||a}$ phase at a film thickness of $\Delta/D_b = 1.75$. Comparing to the analogous plot in Figure 2c, the surface potential has a negligible effect on the central cylinders, but the cylinders along the plates are slightly stretched in the

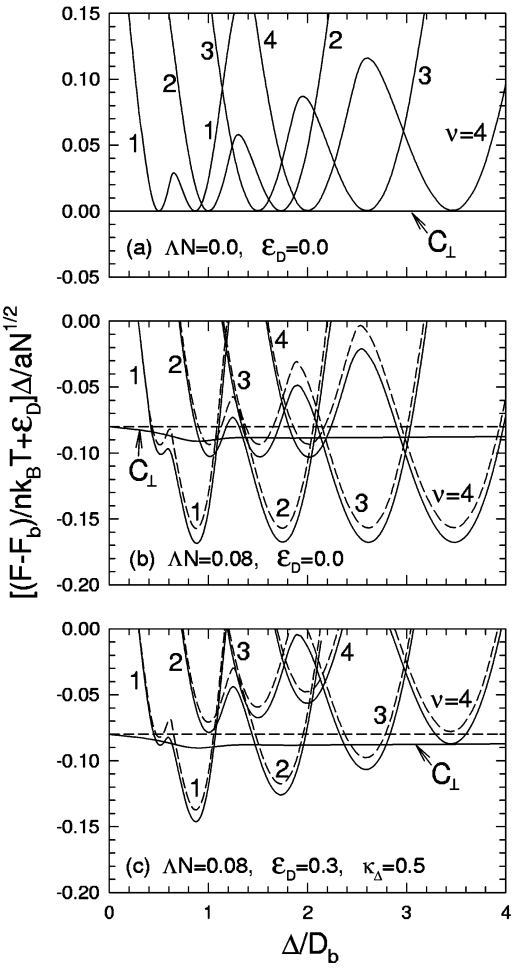


**Figure 6.** Free energy curves for the $C_\perp$ and $C^{\nu}_{\|a}$ phases as a function of film thickness, $\Delta$, (a) without surface affinity and electric field, (b) with surface affinity but without electric field, and (c) with surface affinity and electric field. The dashed curves are approximations based on eq 14. For clarity, the curves for $C^{\nu}_{\|a}$ are just labeled by the total number of cylinder layers, $\nu$.

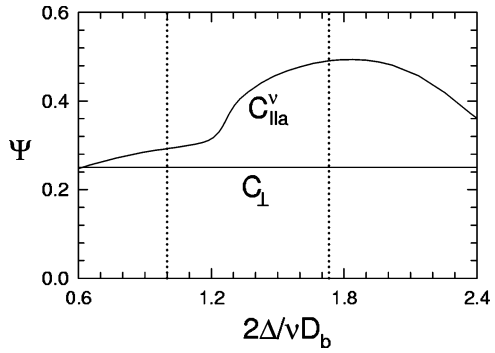


**Figure 7.** A-segment surface coverage, $\Psi$, as a function of film thickness, $\Delta$, for $\Lambda N = \mathcal{C}_D = 0$. The vertical dotted lines denote hexagonal packing.

horizontal direction as indicated by the arrows. Of course, this happens in order to reduce the amount of contact between the B-rich matrix and the plates. An analogous effect occurs for the $C_\perp$ phase, as illustrated in Figure 5b.

The surface affinity, $\Lambda N$, breaks the symmetry among the layers of the $C^{\nu}_{\|a}$ phases, and so their free energies can no longer be represented by a single curve as in Figure 3a. Therefore, Figure 6 plots the free energies as separate curves each as a function of $\Delta/D_b$. For purposes of clarity, the free energy per molecule is multiplied by $\Delta$, and curves for $\nu \geq 5$ are omitted. To provide a reference, Figure 6a replots the previous results for $\Lambda N = \mathcal{C}_D = 0$. This way, one can see the relative positions of the various free energy minima. The solid curves in Figure 6b show the effect of introducing a surface affinity for A-type segments. As expected, this provides a preference for the $C^{\nu}_{\|a}$ phases, but much more so when the cylinder packing is close to the hexagonal arrangement with $2\Delta/\nu = \sqrt{3}D_b$, because the smaller value of $D$ (see Figure 3b) results in a higher concentration of cylinders along the two plates. The solid curves in Figure 6c show the added effect of turning on an electric field. As before, this increases the relative stability of the $C_\perp$ phase, but more so for thicker films because they involve more molecules per unit area.

Because weak surface potentials only have a mild effect on $\phi_A(\mathbf{r})$, we can extend our previous approximation for the free energy to

$$\frac{F}{nk_BT} \approx \frac{F_0}{nk_BT} - 2(\Psi_1\Lambda_1 N + \Psi_2\Lambda_2 N)\frac{aN^{1/2}}{\Delta} - \Omega\mathcal{C}_D \quad (14)$$

where

$$\Psi_1 \equiv \frac{2}{\mathcal{A}}\int d\mathbf{r}\, \delta(z)\phi_A(\mathbf{r}) \quad (15)$$

$$\Psi_2 \equiv \frac{2}{\mathcal{A}}\int d\mathbf{r}\, \delta(z-\Delta)\phi_A(\mathbf{r}) \quad (16)$$

are the A-segment surface coverage at $z = 0$ and $\Delta$, respectively, calculated in the limit of $\Lambda_1 = \Lambda_2 = \mathcal{C}_D = 0$. For completeness, we quote the approximation without assuming the two plates are the same. In our case, however, not only are the plates identical, but the morphologies also possess a symmetry whereby $\Psi_1 = \Psi_2 \equiv \Psi$. This common surface coverage, $\Psi$, is plotted in Figure 7 as a function of film thickness, $\Delta$. For the $C_\perp$ phase, the coverage is simply equal to the diblock composition (i.e., $\Psi = f = 0.25$), but for the $C^{\nu}_{\|a}$ phases, it depends very much on the spacing, $D$, of the cylinders along the plates. Since the hexagonal packing at $2\Delta/\nu = D_b$ has a large lateral spacing of $D = \sqrt{3}D_b$, its surface coverage is only $\Psi \approx 0.3$, while the alternative packing at $2\Delta/\nu = \sqrt{3}D_b$ has a smaller $D = D_b$ and thus larger $\Psi \approx 0.5$. Given Figures 4 and 7, we can now easily anticipate the quantitative effect of $\mathcal{C}_D$ and $\Lambda N$ on the relative stability of the phases. The free energy approximation of eq 14 is shown in Figure 6 with dashed curves, and indeed it is reasonably accurate. The fact that the approximation is obtained by simply neglecting the change in $\phi_A(\mathbf{r})$ caused by $\mathcal{C}_D$ and $\Lambda N$ implies that it is actually an upper bound on the free energy, as clearly evident in Figure 6.

We now repeat our calculations for a surface affinity favoring the matrix ($\Lambda N = -0.12$) sufficient to stabilize the $C^{\nu}_{\|b}$ phases. Figure 8 shows free energy plots for the negative surface affinity analogous to those in Figure 6 for the positive surface affinity. The most notable difference is that the curves for each $C^{\nu}_{\|b}$ phase only display a single minimum corresponding to an approximate hexagonal packing with $2\Delta/\nu \approx \sqrt{3}D_b$ and $D \approx D_b$. The absence of a minimum corresponding to the narrower thickness of $2\Delta/\nu \approx D_b$ and larger lateral periodicity of $D \approx \sqrt{3}D_b$ is a simple consequence of geometry. When $\Delta$ is too small, the gap between the cylinder layers is insufficient to fit a reflecting boundary through the matrix without causing a major distortion to the morphology (see Figure 2a).

The dashed curves in Figure 8 are approximations obtained using eq 14 with $F_0$, $\Omega$, and $\Psi$ taken from Figure 9. Unlike for the $C^{\nu}_{\|a}$ phases, these latter quantities are no longer indepen-

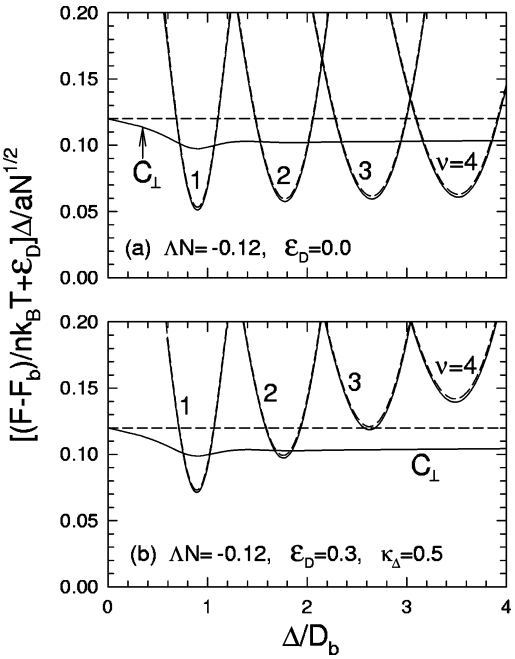


**Figure 8.** Analogous plots to those in Figure 6, but comparing the free energies of the $C_{\perp}$ and $C^{\nu}_{||b}$ phases for plates with an affinity for the matrix component.

dent of $\nu$. The reason is that the different cylinder layers in a $C^{\nu}_{||b}$ phase do not become equivalent in the absence of a surface potential, as they do for a $C^{\nu}_{||b}$ phase. This loss of symmetry occurs because there is no natural symmetry plane through the matrix of the bulk cylinder phase, and thus the reflecting boundary conditions imposed by the plates must be accompanied by a distortion of the cylinders. The fact that this distortion relaxes toward the center of the film breaks the symmetry among the successive cylinder layers. Since $F_0$, $\Omega$, and $\Psi$ need to, therefore, be calculated for each value of $\nu$, the approximation of eq 14 is not quite as economical for the $C^{\nu}_{||b}$ phases as for the $C^{\nu}_{||a}$ phases, but nevertheless it is still very useful.

Undoubtedly, the most effective way of demonstrating the impact of an electric field on the relative stability of the phases is with equilibrium phase diagrams. However, they can be computationally demanding to generate because phase boundaries require matching free energies by adjustment of either the surface affinity, $\Lambda N$, or the electric field strength, $\mathcal{E}_D$. This is where the approximation in eq 14 becomes particularly useful. Figure 10 shows two diagrams mapping the equilibrium phase boundaries between the perpendicular ($C_{\perp}$) and parallel ($C^{\nu}_{||a}$ and $C^{\nu}_{||b}$) morphologies as a function of film thickness, $\Delta$, and surface affinity, $\Lambda N$. The main inaccuracy resulting from our use of eq 14 is a slight overestimation of the $C^{\nu}_{||b}$ regions. Nevertheless, the diagrams provide an excellent illustration of how an applied electric field enhances the size of the $C_{\perp}$ region. A crude estimate for the envelope of the $C_{\perp}$ region, denoted by the dotted lines in Figure 10, is given by the inequality

$$-0.05 - 0.3\tau \gtrsim \Lambda N \gtrsim 0.3\tau \qquad (17)$$

where

$$\tau \equiv \kappa_{\Delta}^{2}\mathcal{E}_{D}\Delta/D_{b} \qquad (18)$$

is the parameter controlling the size of the electric field effect. The effect is stronger for thick films because the electrostatic energy is proportional to the volume $\mathcal{V}$, whereas the surface affinity is only proportional to the area $\mathcal{A}$. Note that the

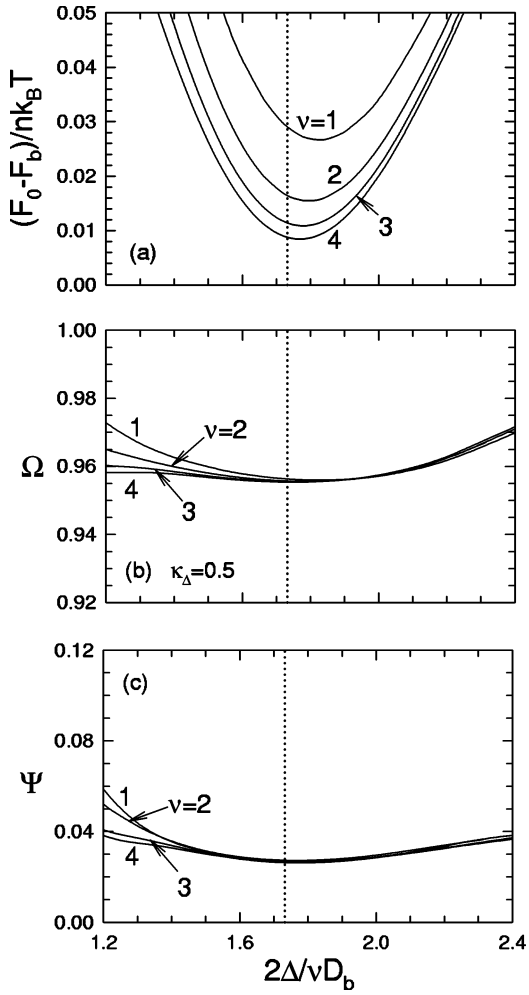


**Figure 9.** Plots for the $C^{\nu}_{||b}$ phases showing (a) the free energy $F_0$, (b) the relative electrostatic energy $\Omega$, and (c) the A-segment surface coverage $\Psi$ calculated in the $\Lambda N = \mathcal{E}_D = 0$ limit for eq 14. The vertical dotted line denotes hexagonal packing for the bulk limit in which the number of cylinder layers, $\nu$, becomes large.

functional form of the inequality in eq 17 will be reasonably general, but the three numerical coefficients are particular to diblocks with a composition of $f = 0.25$ at a segregation of $\chi N = 25$. Nevertheless, we can estimate the effect of segregation using the well-known scaling relations of SST.[23] The first constant in eq 17 should approximately scale as $(\chi N)^{1/2}$, while the two prefactors for $\tau$ should roughly scale as $(\chi N)^{1/6}$.

## IV. Discussion

Our calculations are based on the standard Gaussian chain model[20] supplemented with linear polarizability. The validity of the model relies on a sufficiently high molecular weight to justify the notion of *course-grained* segments and to ensure the distribution of the backbone orientation is sufficiently uniform in a microphase-separated state that the polarizability can be treated as isotropic. This model is then investigated in the mean-field approximation, where each polymer interacts, not with the instantaneous positions of the other molecules, but rather with their average (i.e., mean) positions. Again this is justified when the polymers are of high molecular weight. While these assumptions underlie virtually all theoretical approaches, this is the limit of the approximations used by our SCFT-based treatment. Of course, numerical calculations always involve some numerical uncertainty, but we have taken sufficient care to ensure that it remains irrelevant on the scale of our plots.

There are conditions (e.g., large $\Delta$) where the SCFT calculations become numerically demanding, but still they generally remain within the capabilities of modern desktop computers. Nevertheless, eq 14 offers a welcome reduction in the computational demands of generating phase diagrams like those in Figure 10. With it, the self-consistent-field conditions, eqs 8 and 9, need only be solved for $\Lambda N = \mathscr{C}_D = 0$. As an added bonus, this is the situation for which the calculations are least intensive and also a situation under which all the $C^{\nu}_{\|a}$ solutions become equivalent. Once the fields, $w_A(\mathbf{r})$ and $w_B(\mathbf{r})$, are known, the computational cost of evaluating $F_0$, $\Psi$, and $\Omega$ is trivial. To top it off, the simple form of eq 14 makes it relatively easy to understand the combined effect of the surface affinity and the electric field. In reality, the approximation is merely a first-order Taylor series expansion in terms of $\Lambda_1 N$, $\Lambda_2 N$, and $\mathscr{C}_D$. Indeed, the first-order coefficient for $\mathscr{C}_D$ is given by

$$\frac{dF}{d\mathscr{C}_D} = \frac{\partial F}{\partial \mathscr{C}_D} + \int \left[ \frac{\mathscr{D}F}{\mathscr{D}\phi_A(\mathbf{r})} \frac{d\phi_A(\mathbf{r})}{d\mathscr{C}_D} + \frac{\mathscr{D}F}{\mathscr{D}w_A(\mathbf{r})} \frac{dw_A(\mathbf{r})}{d\mathscr{C}_D} + \frac{\mathscr{D}F}{\mathscr{D}w_B(\mathbf{r})} \frac{dw_B(\mathbf{r})}{d\mathscr{C}_D} \right] d\mathbf{r} \quad (19)$$

Here the exact derivative of $F[\phi_A, w_A, w_B]$ with respect to $\mathscr{C}_D$ equals the partial derivative of $F[\phi_A, w_A, w_B]$ with its three dependent functions fixed plus the integral, which adds the contribution due to the implicit dependence of the three functions on $\mathscr{C}_D$. However, the functional derivatives of $F[\phi_A, w_A, w_B]$ with respect its dependent functions are all zero, since this is the saddle-point condition used to derive the self-consistent-field equations.[18] Thus, the first-order coefficient reduces to

$$\frac{dF}{d\mathscr{C}_D} = \frac{\partial F}{\partial \mathscr{C}_D} = -nk_B T\Omega \quad (20)$$

using eq 2 with $\mathscr{C} = \Omega \mathscr{C}_D$. Likewise, the first-order coefficients for $\Lambda_1 N$ and $\Lambda_2 N$ can also be calculated by disregarding the variations in $\phi_A(\mathbf{r})$, $w_A(\mathbf{r})$, and $w_B(\mathbf{r})$. Although we chose to evaluate these coefficients at $\Lambda_1 N = \Lambda_2 N = \mathscr{C}_D = 0$, the expansion could just as well be carried out about nonzero values of $\Lambda_1 N$, $\Lambda_2 N$, and $\mathscr{C}_D$. Despite that eq 14 is just first order, the only notable inaccuracy occurs because it overlooks the lateral shift in the block copolymer interface caused by the surface interaction (see Figure 5). Incidentally, this effect is just one of the many details ignored by the SST-based calculations.

Although the electric fields in our study were too weak to cause a significant inaccuracy in eq 14, we may not be examining conditions comparable to those of experiment. To gauge whether this is the case, we transform to real units taking $\kappa_A = 5$ and $\kappa_B = 2$ as representative dielectric constants. This corresponds to $\bar{\kappa} \approx 3$ and a dielectric contrast of $\kappa_\Delta \approx 0.5$, which is the particular value that our study focused on. Combining this with typical molecular volumes of $\mathscr{V}/n = 100-1000$ nm$^3$, the $\mathscr{C}_D = 0.3$ used for the phase diagram in Figure 10b converts to applied fields of $E_0 \approx 10-30$ V/$\mu$m, which indeed is comparable to that of experiments.

Our SCFT treatment provides a marked reduction in approximations over the previous calculations based on the strong-stretching theory (SST). In principle, the SST introduces only one extra approximation to make the calculations analytical, that of strongly stretched chains. In practice, however, additional approximations are required to keep the calculations tractable. For example, SST calculations generally assume some a priori shape for the internal interface, whereas SCFT calculations allow the interfacial shape to automatically adjust so as to minimize the free energy. Furthermore, a rigorous treatment of the electric field effects would defeat the simplifications gained by the strong-stretching assumption, and so again more approximations are required by the SST treatment. In contrast, the spectral method for SCFT permits an exact solution to the Maxwell equations with no significant reduction in the efficiency of the algorithm.

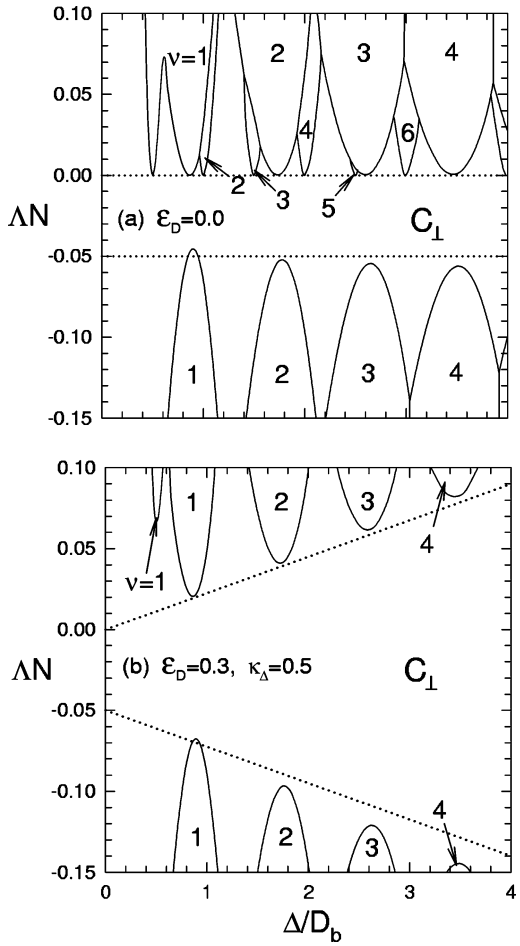


**Figure 10.** Phase diagrams for a melt of diblock copolymers ($f = 0.25$ and $\chi N = 25$) confined between conducting plates with a surface affinity of $\Lambda N$ and a separation of $\Delta$, calculated using the free energy approximation in eq 14. Diagram (a) is without an applied electric field, while diagram (b) is for a field strength of $\mathscr{C}_D = 0.3$ and a dielectric contrast of $\kappa_\Delta = 0.5$. The $C^{\nu}_{\|a}$ phases at $\Lambda N > 0$ and the $C^{\nu}_{\|b}$ phases at $\Lambda N < 0$ are labeled by the total number of cylinder layers, $\nu$. The dotted lines correspond to the inequality in eq 17.

The first SST-based study of applied electric fields on cylinder-forming diblock copolymer films was by Ashok et al.[10] They considered plates with a surface affinity for the matrix component and calculated the effect of the electric field on the phase boundaries between the $C^{\nu}_{\|b}$ and $C_\perp$ morphologies. The merit of their approach is its simplicity, but the resulting level of approximations is severe. For instance, they do not take into account the effect of interfacial curvature on the entropic stretching energy of the A and B blocks. Furthermore, they assume that the cylinders of the $C^{\nu}_{\|b}$ phases are perfectly circular with a radius of $r$ and that the packing is always hexagonal with a nearest-neighbor spacing of $2R$. The description of their derivation is very sketchy, but evidently it does not even enforce the conservation of the domain volumes, which requires $\pi r^2 = 2\sqrt{3}R^2 f$. The electrostatic energy is also calculated under an assumption that each cylinder can be treated

in isolation, which at the very least ignores the contribution to $\mathcal{E}$ resulting from the overlap of their induced electric fields.

Pereira[12] provides another SST-based treatment, but this time examining the relative stability of the $C^{\nu}_{\|a}$ and $C_{\perp}$ phases, which compete for stability when the plates have an affinity for the minority domain. His study is much more sophisticated and extensive than that of Ashok et al. First, Pereira allows the cylinders of the $C^{\nu}_{\|a}$ phases to deviate from hexagonal packing, assuming that it accompanied by an affine deformation of the interfacial shape. Because his calculation is based on deformed hexagonal unit cells, he views the two orientations in Figure 3 (i.e., $2\Delta/\nu = D_b$ and $\sqrt{3}D_b$) as separate phases, $\nu$CI and $\nu$CII, respectively; this, however, is a rather minor issue. Second, Pereira performs a more rigorous treatment of the stretching energy, but nevertheless one where the connection between the A and B blocks is not enforced.[25] However, this approach predicts an instability in the hexagonal symmetry, which even affects the bulk phase.[24] As a consequence, his free energy minima for $\nu$CI and $\nu$CII, corresponding to our two minima in Figure 3a, both bifurcate into double minima. It has since been demonstrated that the instability is a direct consequence of not enforcing the connectivity of the diblock.[26] When it is enforced by, for example, applying the wedge approach of Olmsted and Milner,[27] this anomalous behavior vanishes. Unfortunately, Pereira encounters further problems with his treatment of the applied field. He considers two separate lines of approximation: a *capacitor analogy* that assumes the electric field remains perpendicular to the film and an *electric field distortion* approximation similar to that used by Ashok et al. The problem is that the two approaches produced inconsistent results. For cylinders consisting of the low-dielectric component, the capacitor analogy predicts the electric field to favor the perpendicular orientation, while the electric field distortion approach predicts it to favor the parallel orientation. From our SCFT results, we now know that the latter prediction is wrong, which casts further doubts on the reliability of the Ashok et al. calculation given its similar treatment of the electric field.

We note that Xu et al.[4] have performed some SCFT-based calculations to model their experimental observations, but their theoretical study did not investigate the equilibrium behavior as we have. Instead, they performed dynamical simulations to mimic the mechanism by which the cylinders flip between parallel and perpendicular orientations. Furthermore, their study only focused on qualitative behavior, perhaps because the large size of their simulation box forced them to use course meshes in their real-space calculations, which must result in a significant degree of numerical inaccuracy. In addition, they also used an approximate treatment for the electric field.

One thing we can never be certain of with mean-field calculations, which includes both SST and SCFT, is whether all possible equilibrium phases have been considered. Some experiments[28] involving plates with a strong affinity for the minority component observe a relatively flat monolayer along the surfaces, as opposed to the series of half cylinders in the $C^{\nu}_{\|a}$ phases. The advantage is that the A-segment surface coverage becomes $\Psi \approx 1$, but there is also a disadvantage associated with the loss of interfacial curvature. We have tested for this phase and found it to be highly unstable over our range of parameters, although it is certain to become stable at larger values of $\Lambda N$ or at values of $f$ closer to 0.5. Other experiments[29] have observed a morphology at small $\Delta$ where the minority domain appears to form a perforated lamella, as supported by SCFT-based simulations[29] and by lattice-based Monte Carlo simulations.[30] However, these studies are at much larger diblock compositions (e.g., $f \approx 0.33$), where block copolymers are well-known for producing perforated lamellae.[31] Earlier experimental studies on symmetric diblocks reported morphologies containing a mixture of perpendicular and parallel lamellae,[32] but SCFT calculations[16] predict that these are only metastable nanostructures. To our knowledge, analogous phases have never been observed for cylinder-forming diblocks, nor do we expect them because of the extra degree of freedom cylinders have to relieve packing frustration by adjusting their lateral spacing (i.e., $D$). Furthermore, the level of packing frustration produced by confinement never gets that large for $\Lambda N < 0$ because the cylinders have two distinct hexagonal arrangements (i.e., $2\Delta/\nu = D_b$ and $\sqrt{3}D_b$) to choose from. Thus, we can be reasonably confident that no morphologies are missing from our equilibrium phase diagrams in Figure 10.

A useful feature of the SCFT-based approach, which we have yet to mention, is its impressive versatility. Although we have maintained the same simple model of the preceding SST calculations so as to compare like with like and to keep the number of system parameters to a manageable level, the theory can readily be extended to account for polydispersity,[33] conformational asymmetry,[34] compressibility,[35] and other similar effects. It is also straightforward to generalize the functional forms for the surface potential $H(\mathbf{r})$, the electric permittivity $\kappa(\mathbf{r})$, and the A−B segment interaction $\chi\phi_A(\mathbf{r})\phi_B(\mathbf{r})$.[20] The theory can also cope with complex block copolymer architectures such as linear multiblocks, combs, stars, and so on.[36] Furthermore, there is no problem in accounting for additional species such as added homopolymer or solvent.[37] Even if some of the species were charged,[6] this could be handled by generalizing the Maxwell equation to $\nabla\cdot(\kappa\mathbf{E}) = \rho_f/\epsilon_0$, where $\rho_f$ is their total charge density.

## V. Conclusions

We have investigated the equilibrium phase behavior of cylinder-forming diblock copolymer confined between two parallel conducting plates with a surface affinity of $\Lambda$, separated by a distance $\Delta$, and maintained at a potential difference of $V_0$ (see Figure 1). Our calculations are based on an exact mean-field treatment using SCFT, where the electrostatic energy is obtained by an exact solution to the Maxwell equations. This removes the myriad of approximations and assumptions implemented by previous mean-field calculations using SST. Although the SCFT-based calculations are numerical rather than analytical, we have demonstrated that the computational demands of generating phase diagrams (see Figure 10) can be significantly reduced by a linear expansion in the surface potential, $\Lambda N$, and the electric field strength, $\mathcal{E}_D$ (see eq 14). The most significant source of inaccuracy is that it ignores the shift in the block copolymer interface along the plates caused by the surface affinity (see Figure 5). Nevertheless, the expansion provides a reasonable quantitative approximation as well as valuable insights into how $\Lambda N$ and $\mathcal{E}_D$ affect the stability of perpendicular cylinders, which is conveniently summed up by the simple inequality in eq 17.

## References and Notes

(1) Russell, T. P. *Curr. Opin. Colloid Interface Sci.* **1996**, *1*, 107. Matsen, M. W. *Curr. Opin. Colloid Interface Sci.* **1998**, *3*, 40. Hamley, I. W. *Nanotechnology* **2003**, *14*, R39. Segalman, R. A. *Mater. Sci. Eng. R* **2005**, *48*, 191.

(2) Amundson, K.; Helfand, E.; Davis, D. D.; Quan, X.; Patel, S. S.; Smith, S. D. *Macromolecules* **1991**, *24*, 6546. Amundson, K.; Helfand, E.; Quan, X.; Smith, S. D. *Macromolecules* **1993**, *26*, 2698. Amundson, K.; Helfand, E.; Quan, X.; Hudson, S. D.; Smith, S. D. *Macromolecules* **1994**, *27*, 6559.

(3) Xu, T.; Hawker, J.; Russell, T. P. *Macromolecules* **2003**, *36*, 6178.
(4) Xu, T.; Zvelindovsky, A. V.; Sevink, G. J. A.; Lyakhova, K. S.; Jinnai, H.; Russell, T. P. *Macromolecules* **2005**, *38*, 10788.
(5) Thurn-Albrecht, T.; DeRouchey, J.; Russell, T. P.; Kolb, R. *Macromolecules* **2002**, *35*, 8106.
(6) Tsori, Y.; Tournilhac, F.; Andelman, D.; Leibler, L. *Phys. Rev. Lett.* **2003**, *90*, 145504. Tsori, Y.; Tournilhac, F.; Leibler, L. *Macromolecules* **2003**, *36*, 5873.
(7) Wang, J.-Y.; Xu, T.; Leiston-Belanger, J. M.; Gupta, S.; Russell, T. P. *Phys. Rev. Lett.* **2006**, *96*, 128301; curve (a) in Figure 3 shows a weak frequency dependence for the dielectric constant of normal PMMA, suggesting that the concentration of free ions is relatively insignificant.
(8) Pereira, G. G.; Williams, D. R. M. *Macromolecules* **1999**, *32*, 8115.
(9) Semenov, A. N. *Sov. Phys. JETP* **1985**, *61*, 733.
(10) Ashok, B.; Muthukumar, M.; Russell, T. P. *J. Chem. Phys.* **2001**, *115*, 1559.
(11) Tsori, Y.; Andelman, D. *Macromolecules* **2002**, *35*, 5161.
(12) Pereira, G. G. *Eur. Phys. J. E* **2002**, *7*, 273.
(13) Helfand, E. *J. Chem. Phys.* **1975**, *62*, 999.
(14) Matsen, M. W. *J. Chem. Phys.* **2006**, *124*, 074906.
(15) Matsen, M. W. *Phys. Rev. Lett.* **2005**, *95*, 258302. Lin, C.-L.; Schick, M.; Andelman, D. *Macromolecules* **2005**, *38*, 5766. Tsori, Y.; Andelman, D.; Lin, C.-Y.; Schick, M. *Macromolecules* **2006**, *39*, 289.
(16) Matsen, M. W. *J. Chem. Phys.* **1997**, *106*, 7781.
(17) Note that a factor of 4 is missing from eq 5 in ref 16 for the surface potential, $H(\mathbf{r})$.
(18) Matsen, M. W. In *Soft Matter*; Gompper, G., Schick, M., Eds.; Wiley-VCH: Weinheim, Germany, 2006; Vol. 1.
(19) Silberberg, A. *J. Colloid Interface Sci.* **1982**, *90*, 86.
(20) Matsen, M. W. *J. Phys.: Condens. Matter* **2002**, *14*, R21.
(21) Orzechowski, K. *Chem. Phys.* **1999**, *240*, 275.
(22) Matsen, M. W.; Bates, F. S. *J. Chem. Phys.* **1997**, *106*, 2436.
(23) In SST,[9] domain sizes scale as $(\chi N)^{1/6}$, interfacial tension increases as $(\chi N)^{1/2}$, and energy per molecule varies as $(\chi N)^{1/3}$.
(24) Pereira, G. G. *Phys. Rev. E* **2001**, *63*, 061809.
(25) Likhtmann, A. E.; Semenov, A. N. *Macromolecules* **1997**, *30*, 7273.
(26) Matsen, M. W. *Phys. Rev. E* **2003**, *67*, 023801.
(27) Olmsted, P. D.; Milner, S. T. *Macromolecules* **1998**, *31*, 4011.
(28) Mansky, P.; Chaikin, P.; Thomas, E. L. *J. Mater. Sci.* **1995**, *30*, 1987.
(29) Knoll, A.; Horvat, A.; Lyakhova, K. S.; Krausch, G.; Sevink, G. J. A.; Zvelindovsky, A. V.; Magerle, R. *Phys. Rev. Lett.* **2002**, *89*, 035501.
(30) Szamel, G.; Müller, M. *J. Chem. Phys.* **2003**, *118*, 905.
(31) Hamley, I. W.; Koppi, K. A.; Rosedale, J. H.; Bates, F. S.; Almdal, K.; Mortensen, K. *Macromolecules* **1993**, *26*, 5959. Hajduk, D. A.; Takenouchi, H.; Hillmyer, M. A.; Bates, F. S.; Vigild, M. E.; Almdal, K. *Macromolecules* **1997**, *30*, 3788.
(32) Koneripalli, N.; Levicky, R.; Bates, F. S.; Ankner, J.; Kaiser, H.; Satija, K. *Langmuir* **1996**, *12*, 6681.
(33) Sides, S. W.; Fredrickson, G. H. *J. Chem. Phys.* **2004**, *121*, 4974.
(34) Matsen, M. W.; Bates, F. S. *J. Polym. Sci., Part B* **1997**, *35*, 945.
(35) Helfand, E.; Tagami, Y. *J. Chem. Phys.* **1972**, *56*, 3592.
(36) Matsen, M. W.; Schick, M. *Macromolecules* **1994**, *27*, 6761; *Macromolecules* **1994**, *27*, 7157.
(37) Hong, K. M.; Noolandi, J. *Macromolecules* **1981**, *14*, 727. Matsen, M. W. *Phys. Rev. Lett.* **1995**, *74*, 4225.

MA060456M